AIAA JOURNAL
Vol. 31, No. 11, November 1993

Two-Beam Multiplexed Laser-Induced Fluorescence Measurements of an Argon Arcjet Plume

Wilhelmus M. Ruyten*
University of Tennessee—Calspan Center for Space Transportation and Applied Research, Tullahoma, Tennessee 37388
and
Dennis Keefer†
University of Tennessee Space Institute, Tullahoma, Tennessee 37388

We describe a multiplexed, laser-induced fluorescence (LIF) technique with which radial and axial profiles of vector velocities of excited propellant species were obtained in the exhaust plume from a 300-W argon arcjet. Although the arcjet is a prototype, and although argon is not an interesting propellant from a propulsion perspective, the technique clearly demonstrates how a narrowband, frequency-stabilized ring-dye laser can be used to obtain simultaneous measurements of two velocity components in an arcjet plume and how a third signal from an optogalvanic cell can be used as a frequency reference. We also show that much information on the flow can be obtained by analyzing the Doppler widths and fluorescence intensities of the LIF data. Specifically, the data identify a boundary layer in the radial direction of the plume and a shock in the downstream region of the flow. Also, some flow anisotropy is observed, consistent with the assumption that the magnitude of the mean flow velocity fluctuates. The peak velocity on centerline remains roughly constant at 3 km/s throughout the expansion.

I. Introduction

RECENT studies have re-emphasized that significant savings in satellite launch costs can be realized by using electric propulsion systems for orbit transfer and station keeping.[1,2] Although the concepts of many of these thrusters have been known for almost three decades,[3] development has been delayed due to a lack of adequate space power and appropriate missions. As a result, several types of thrusters are only now reaching the level of maturity required for deployment.[4,5]

Early development and optimization of electric thrusters has taken place largely by empirical methods, but new computational methods are becoming available to permit a more systematic approach to optimize thruster performance.[6-8] However, it is a considerable challenge to model accurately the properties of the plasma core and the exhaust plume of, for example, an arcjet thruster. Thermodynamic and transport properties of some of the relevant processes are difficult to calculate or measure for the temperatures and pressures of interest. Thus code validation can only be achieved with the help of detailed measurements of the plume properties at the exit nozzle. In this paper, we describe a laser-induced fluorescence (LIF) technique that is capable of producing such data. Specifically, we report spatially resolved measurements of the exit vector velocities, Doppler widths, and fluorescence intensities of propellant species in the exhaust plume from a low-power (300-W) argon arcjet.

The principle of measuring flow velocities using LIF has been known for some time. For example, Zimmerman and Miles[9] developed an LIF technique for measuring velocities in a hypersonic wind tunnel a decade ago. The technique consists of using a narrowband laser to excite one of the plume species, and fluorescence radiation is detected as an indicator of the absorption process. Unlike in emission spectroscopy,[10-13] a small effective scattering volume can be defined by imaging only a small section of a focused laser beam onto a detector. Thus spatial resolution on the order of a millimeter or less is easily achieved. By tuning the laser across the absorption profile of the absorbing species, the Doppler profile of the transition is obtained, which is essentially given by the velocity distribution of the absorbing species projected onto the propagation direction of the laser beam.

Quite recently, several groups have used LIF techniques to measure flow velocities in the exhaust plumes from a 30-kW class hydrazine arcjet[14] and from a 1-kW class hydrogen arcjet.[15-18] In both cases, excitation of the hydrogen Balmer-α line was used to extract radial profiles of the axial velocity components in the flow. Also, some qualitative features of the distribution of Doppler widths and fluorescence intensities were discussed, but no detailed data were presented.

Here we describe an LIF scheme that is similar to those mentioned earlier, except, by two-beam multiplexing, we are able to measure radial and axial velocity components in the flow simultaneously. We also demonstrate how an optogalvanic cell can be used to obtain a simultaneous reference signal for frequency calibration[19] and how an analysis of the distributions of Doppler widths and fluorescence intensities can be used to identify such features as boundary layers and shocks in the flow. The choice of argon propellant was mostly for convenience, and some of the data may not be representative for a higher power hydrazine or hydrogen arcjet. However, the technique itself should be applicable to such systems without much modification.

The outline of the paper is as follows. In Sec. II, the theory is developed that forms the basis for analyzing the multiplexed LIF data. In Sec. III, the experimental facilities are described. In Sec. IV, the results of radial and axial plume measurements are presented. A discussion and summary are presented in Sec. V, as well as a comparison with some of the previous arcjet LIF work. Other, somewhat more extensive accounts of this work may be found in Refs. 20 and 21. Also, a preliminary comparison of our experimental results with those from a numerical model have been presented.[22]

Based on Paper 91-093 presented at the 22nd International Electric Propulsion Conference, Viareggio, Italy, Oct. 14–17, 1991; received Jan. 14, 1992; revision received Nov. 25, 1992; accepted for publication Nov. 25, 1992. Copyright © 1993 by the American Institute of Aeronautics and Astronautics, Inc. All rights reserved.

*Research Physicist, UTSI Research Park; also Calspan Corporation, AEDC Operations. Member AIAA.

†B. H. Goethert Professor ES&M, Center for Laser Applications. Member AIAA.

II. Theory

In this section, we consider the problem of determining the properties of the velocity distribution function of the propellant plume, in two dimensions, from Doppler measurements along two nonorthogonal laser beam directions in the experiment.

To start, we assume that the distribution of velocities of the species that is excited in the LIF scheme is fully characterized by the distribution function $f(v_x, v_y)$, where v_x and v_y are the velocity components along two orthogonal axes, namely, parallel and perpendicular to the arcjet centerline. With proper normalization, the density n_a of the absorbing species is given by the zeroth moment of this distribution function:

$$n_a = \iint f(v_x, v_y)\, \mathrm{d}v_x\, \mathrm{d}v_y \tag{1}$$

(Unless noted otherwise, all integrals are from $-\infty$ to $+\infty$.) The mean velocity components $\overline{v_x}$ and $\overline{v_y}$ are given by the first moments of the distribution function:

$$\overline{v_{x,y}} = \frac{1}{n_a} \iint v_{x,y} f(v_x, v_y)\, \mathrm{d}v_x\, \mathrm{d}v_y \tag{2}$$

Similarly, the variances and covariance are given by the second central moments of the distribution function.[20] For the general case of a nonisotropic distribution, a rotated coordinate system can be defined in which the covariance vanishes. If we denote the variances along the rotated axes by $\sigma_\parallel^2$ and $\sigma_\perp^2$, we can interpret such a nonisotropic distribution as an elliptical distribution with major axes of radii $\sigma_\parallel$ and $\sigma_\perp$ at an angle γ to the original coordinate system (see Fig. 1). For an isotropic distribution, $\sigma_\parallel^2 = \sigma_\perp^2$ and the angle γ is undefined.

Now let us consider an LIF measurement, in which a narrowband laser beam intersects the plume at an angle φ to the centerline (in Fig. 1, the wave vector $\boldsymbol{k}_\varphi$, associated with the laser beam, is shown). Excitation of the gas occurs when the Doppler shift of the absorbing atom is equal to and opposite the detuning of the laser from line center. In terms of velocity, this resonance condition for the Doppler shift ν_D may be expressed as

$$\nu_D = -\lambda(\nu_L - \nu_0) \tag{3}$$

where λ is the wavelength of the transition, and $\nu_L - \nu_0$ is the detuning of the laser frequency ν_L from the centerline frequency ν_0. More precisely, excitation of the gas takes place if the detuning from Doppler-shifted line center is less than the homogeneous line width of the excitation process. In the experiment, this homogeneous line width is much less than the Doppler width of the velocity distribution of interest. In particular, the laser line width is three orders of magnitude

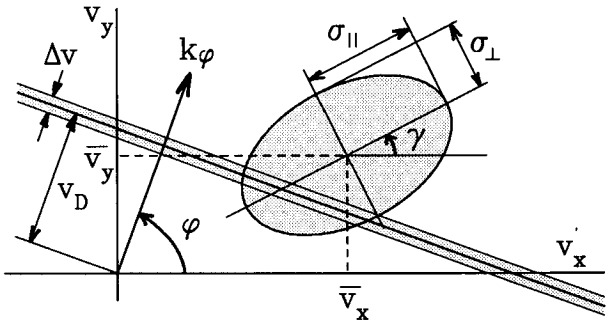

Fig. 1 Schematic representation of a general, two-component velocity distribution function, with mean velocities $\overline{v_x}$ and $\overline{v_y}$, widths $\sigma_\parallel$ and $\sigma_\perp$, and orientation angle γ. The rectangular band of width $\Delta\nu$ encloses velocities with equal Doppler shifts ν_D. For a laser beam angle φ, this is the group of atoms whose velocity vectors are perpendicular to the wave vector k_φ of the laser beam, shown also.

smaller than typical Doppler widths of the species in the plume. Also, the laser power density in the excitation volume is sufficiently small that no significant power broadening and saturation of the transition occur. Thus, the LIF signal, for a laser beam at an angle φ to the centerline, may be expressed as

$$S_\varphi(\nu_D) = C_\varphi \iint_{\text{band}} f(v_x, v_y)\, \mathrm{d}v_x\, \mathrm{d}v_y \tag{4}$$

where C_φ is an experiment-dependent constant. The "band" of integration in Eq. (4) is shown schematically in Fig. 1. It is given by the Doppler resonance condition

$$|v_x \cos\varphi + v_y \sin\varphi - \nu_D| < \tfrac{1}{2}\Delta\nu \tag{5}$$

where ν_D is the Doppler velocity from Eq. (3), $\Delta v = \lambda\Delta\nu$, and $\Delta\nu$ is the small homogeneous line width of the excitation process. It has been explicitly indicated in Eq. (4) that the LIF signal $S_\varphi(\nu_D)$ is obtained as a scan across the absorption profile of the transition or, with Eq. (3), across the Doppler distribution projected onto the laser beam.

To proceed, it is convenient to assume a specific model function for the velocity distribution function $f(v_x, v_y)$ of the absorbing species. Let us first consider the two-dimensional, Gaussian distribution function

$$f(v_x, v_y) = \frac{n_a}{\pi\sigma_\parallel \sigma_\perp} \exp\left[-\left(\frac{v_x - \overline{v_x}}{\sigma_\parallel}\right)^2 - \left(\frac{v_y - \overline{v_y}}{\sigma_\perp}\right)^2 \right] \tag{6}$$

which is normalized according to Eq. (1) and has mean velocities $\overline{v_x}$ and $\overline{v_y}$ that satisfy Eq. (2). Substitution of this model function into Eq. (4) and integration over the velocity band from Eq. (5) yield the corresponding Doppler profile at angle φ:

$$S_\varphi(\nu_D) = A_\varphi \exp\left[-\left(\frac{\nu_D - \nu_\varphi}{\sigma_\varphi}\right)^2 \right] \tag{7}$$

where

$$A_\varphi = \pi^{-1/2} n_a C_\varphi \Delta\nu / \sigma_\varphi \tag{8}$$

$$\nu_\varphi = \overline{v_x} \cos\varphi + \overline{v_y} \sin\varphi \tag{9}$$

and

$$\sigma_\varphi^2 = \sigma_\parallel^2 \cos^2\varphi + \sigma_\perp^2 \sin^2\varphi \tag{10}$$

That is, the Doppler profile is a Gaussian also, with an amplitude, center, and width that depend on the laser angle φ. Allowing for the more general case in which the Gaussian distribution from Eq. (6) is oriented at an angle γ to the v_x axis, it can be shown that the Doppler profile $S_\varphi(\nu_D)$ is still given by Eq. (7), with an amplitude as in Eq. (8), a mean velocity ν_φ as in Eq. (9), but with a variance σ_φ^2 that is now given by

$$\sigma_\varphi^2 = \sigma_\parallel^2 \cos^2(\varphi - \gamma) + \sigma_\perp^2 \sin^2(\varphi - \gamma) \tag{11}$$

That is, the variance of the Doppler profile depends on the laser angle relative to the orientation angle of the velocity distribution.

In the experiment, Doppler profiles are obtained simultaneously perpendicular to the flow ($\varphi = 90$ deg) and at an angle $\varphi = \alpha \simeq 76$ deg. By fitting the two profiles to Gaussian model functions of the general form of Eq. (7), we thus obtain, for each Doppler profile, a mean shift ν_φ, a variance σ_φ^2, and an integrated signal N_φ, given by

$$N_\varphi = \int S_\varphi(\nu_D)\, \mathrm{d}\nu_D = \pi^{1/2} A_\varphi \sigma_\varphi \tag{12}$$

In principle, it is possible to obtain the density n_a of the absorbing species from the integrated signal N_φ. This, however, would require an absolute calibration of the experiment constants C_φ and $\Delta\nu$ from Eq. (8), which is not easily accomplished. Still, measurement of N_φ at different positions in the flow gives an indication of the relative density variations of the absorbing species in the flowfield. By contrast, interpretation of the mean velocities and variances is relatively straightforward. Namely, if we denote the fitted mean velocities by ν_{90} and ν_α, we note that, by Eq. (9), ν_{90} is just the mean velocity component $\overline{v_y}$ in the radial direction and that the mean axial velocity component $\overline{v_x}$ follows from

$$\overline{v_x} = (\nu_\alpha - \nu_{90}\sin\alpha)/\cos\alpha \tag{13}$$

Similarly, the data yield two values of the fitted variances, namely, σ_{90}^2 and σ_α^2. In the experiment, there appears to exist a small systematic difference between the two values. Although measurement at a third angle φ would be required to determine both the variances $\sigma_\parallel^2$ and $\sigma_\perp^2$, as well as the orientation angle γ of the distribution, we find that the data are consistent with the assumption that the orientation angle γ is equal to the flow direction β, which is given by

$$\tan\beta = \overline{v_y}/\overline{v_x} \tag{14}$$

To demonstrate this correlation, we use the expression

$$\left(\frac{\sigma_\alpha}{\sigma_{90}}\right)^2 - 1 = \mathfrak{R}\cos\alpha\cos(\alpha - 2\beta) \tag{15}$$

with

$$\mathfrak{R} = \left(\frac{\sigma_\parallel}{\sigma_\perp}\right)^2 - 1 \tag{16}$$

This result may be obtained from Eq. (11) for small flow angles β, for which $\mathfrak{R}\sin^2\beta \ll 1$. The resulting ratio of parallel to perpendicular variances, however, is rather large ($\sigma_\parallel/\sigma_\perp \simeq 2.78$). Moreover, the ratio appears to remain fairly constant throughout the expansion. In the Appendix we show that the same correlation between width ratios and flow angles can also be accounted for by an alternative assumption, namely, that the velocity distribution itself is isotropic but has a mean flow velocity whose magnitude fluctuates on a time scale that is not resolved in the experiment. In this case, the correlation between Doppler widths and flow angles can, again, be expressed by Eq. (15). But the coefficient $\mathfrak{R}$ is now given by

$$\mathfrak{R} = \left(\frac{\overline{\Delta v}}{\sigma}\right)^2 - 1 \tag{17}$$

where $\overline{\Delta v}^2$ is the variance of the temporal fluctuations in the magnitude of the mean velocity, and σ^2 is the variance of the isotropic velocity distribution. Although this model accounts for the observed difference in Doppler widths at the two laser beam angles, more experiments are required to resolve the issue.

Because of the observed plume fluctuations, some further care must be exercised in the interpretation of the data. Particularly, a measured variance σ^2 may lead to an overestimate of the Doppler temperature. This temperature T is related to the variance σ^2 of the velocity distribution by

$$kT = \tfrac{1}{2}m\sigma^2 \tag{18a}$$

or to the full-width half-maximum, $\Delta\nu_D$, of the measured Doppler profile by

$$\Delta\nu_D = \sqrt{\frac{8kT\ln 2}{m\lambda^2}} \tag{18b}$$

where m is the atomic mass of the absorbing species, k is Boltzmann's constant, and λ is the wavelength of the optical transition from Eq. (3). Similarly, other broadening mechanisms may lead to overestimates of the Doppler temperature. For example, in Refs. 14 and 15, laser power broadening was shown to be significant, and with the pulsed laser technique used in Ref. 14, laser line width broadening was substantial as well. In addition, Stark broadening of the absorption process due to electrons in the plume is more serious for hydrogen than it is for argon, as is broadening due to fine-structure components within the absorption line. As remarked earlier, we believe that neither power broadening, nor saturation broadening, nor other types of broadening contribute significantly to the observed Doppler widths of our data, with the possible exception of broadening due to averaging over plume fluctuations.

III. Description of the Experiment

Arcjet and Vacuum Facility

The arcjet was built locally, based on the same design parameters as the familiar low-power arcjet that has been tested extensively at NASA Lewis Research Center.[23] A cutaway cross section is shown in Fig. 2. The cathode, made out of thoriated tungsten, has a diameter of 3.2 mm and a half-tip angle of 30 deg and is centered inside a copper anode nozzle with a boron nitride insulator. The water-cooled anode section has a 0.5-mm-long constrictor channel with a diameter of 0.5 mm and conical sections upstream and downstream of the constrictor with half-angles of 30 and 20 deg, respectively. The length of the expansion region is 9.5 mm, yielding a nozzle exit radius of 3.7 mm and a nozzle expansion ratio of about 200. The anode-cathode gap is adjustable but was maintained at a constant value of 0.60 mm. Propellant is injected tangentially through helical grooves in the boron nitride insulator.

Operating conditions of the thruster were as follows. Standard purity argon (UN 1006) was used. The flow rate was set to 135 mg/s but could not be controlled actively, allowing variations in flow rate of up to 5%. Using an adjustable power supply, the arc current was maintained at 10 A, yielding a corresponding arc voltage of 32 V.

The vacuum chamber has a main section that is 6.0 m long and 2.7 m wide, with a smaller section on one end, in which the arcjet was mounted. The thruster could be maneuvered in three orthogonal directions with a computer-controlled xyz stage that has a range of travel of 0.3 m in each direction and a positioning accuracy of better than 0.05 mm. The pumping for these experiments was performed by a Stokes Microvac pump equipped with a blower, yielding a pumping speed of 110 l/s. During steady-state operation, the vacuum level in the test facility was about 40 Pa (0.3 Torr).

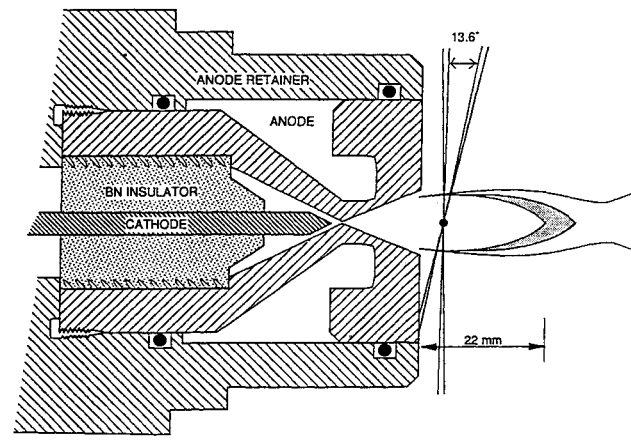

Fig. 2 Schematic of the arcjet and of a typical plume pattern as it appears to the eye. The small circle at the crossing of the two laser beams represents the detection volume, as defined by the collection optics.

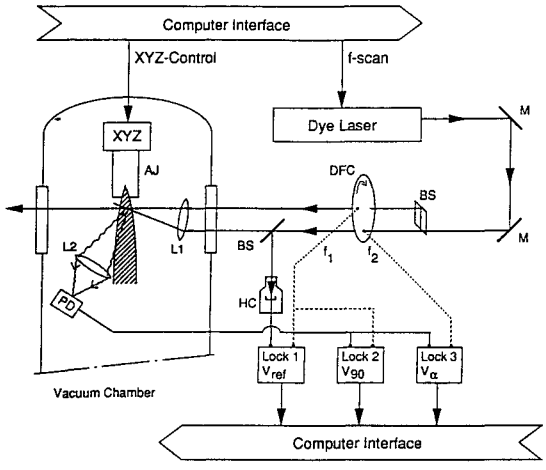

Fig. 3 Schematic of the complete LIF setup: M = mirror, BS = beam splitter, DFC = dual frequency chopper, HC = hollow cathode lamp, $L1$ = focusing lens, $L2$ = collection lens, PD = photodiode (with pinhole aperture), AJ = arcjet, and LOCK = phase-locked amplifier. Not shown is a wave meter that is used to tune the laser to the desired absorption line.

One undesirable feature of the experiment was that of significant fluctuations ("jumps") of the arcjet plume. These occurred on a time scale of one to several seconds and could not be significantly reduced by adjusting any of the operating conditions of the thruster. Fluctuations in the arc voltage were also observed and seemed to correlate with the visual fluctuations in the plume. Despite these fluctuations, reasonable LIF data could be obtained. However, we expect that significantly better signal-to-noise ratios would be possible for a steadier plume.

Laser Diagnostics Setup

A schematic of the optical setup is shown in Fig. 3. The main component is a tunable ring-dye laser (coherent model CR-699), with a line width of approximately 1 MHz and a frequency drift on the order of 0.3 GHz/h. The argon absorption line used in this work was the 727.3-nm line, which, although not a metastable line, originates from an excited species of the neutral argon atom ($1s_4$–$2p_2$ in Paschen notation[24]). In a separate experiment, not reported here, it was verified that the signal levels, as well as the calculated mean velocities and variances of the corresponding Doppler profiles, were roughly the same for the 727.3-nm line as for the metastable line at 714.7 nm ($1s_5$–$2p_4$ transition), indicating that the densities in the arcjet plume must be sufficiently high that the nonmetastable $1s_4$ level is strongly coupled by collisions to the $1s_5$ metastable level.

A small fraction of the dye laser beam is split off into a wave meter, to aid in tuning the laser to the desired absorption line. The remainder of the beam is split into two parallel beams of equal intensity and chopped at frequencies of 400 and 333 Hz with a dual frequency chopper. A further small fraction of one of the beams is split off and directed into a hollow cathode discharge lamp to obtain an optogalvanic reference signal. Thus, as the laser is tuned through the line center of the argon buffer gas in the lamp, a small change in the lamp current results, which is easily detected with the help of a phase-locked amplifier.[25]

The purpose of the optogalvanic reference signal is twofold. First, it provides a very convenient means of fine-tuning the dye laser to the desired absorption line. But, more importantly, it provides an accurate, independent measurement of the non-Doppler-shifted line center ν_0 from Eq. (3). By contrast, in Refs. 14 and 15, line center is assumed to be given by the center of the radial velocity distribution of the arcjet plume. Just like the LIF signal, the optogalvanic reference signal gives rise to a Doppler profile. This signal is recorded simultaneously with the two LIF signals from the arcjet plume, as illustrated in Fig. 4. In a separate series of calibration measurements, described elsewhere,[19] it was determined that the true, unshifted line center ν_0 for the operating conditions in this experiment was actually located at $\nu_{ref} - 30$ MHz $\pm$ 10 MHz, where ν_{ref} is the curve-fitted line center of the optogalvanic Doppler profile. This 30-MHz shift is the result of a small drift velocity of neutral atoms in the discharge lamp.

To obtain the LIF signals, the two parallel laser beams are directed into the vacuum chamber and are focused by a 125-mm lens inside the chamber so that the two beams overlap near the arcjet nozzle exit at a relative angle of $\alpha' \equiv 90$ deg $- \alpha = 13.6$ deg. This angle is large enough to calculate the axial velocity component reliably using Eq. (13), but it is not so large that greatly different Doppler shifts result for the two beams. One of the two beams is parallel to the nozzle exit plane (see Fig. 2), whereas the other strikes the nozzle exit surface obliquely; the resulting scattering proved negligible.

For excitation at 727.3 nm, the fluorescence consists primarily of lines at 810.8, 772.4, and 696.5 nm.[24] Using a 100-mm focal length lens with a diameter of 50 mm, the fluorescence is collected perpendicular to the plane in which the two laser beams cross. The light is focused onto a photodiode with a good spectral response in the 700–900 nm range (Hamamatsu model S-1722-02). Unit magnification of the detection system is used, so that the effective size of the collection volume at the overlap of the two laser beams is equal to the diameter of the pinhole on the photodiode, which was 1 mm. Thus, the spatial resolution of the data along the direction of the laser beams is about 1 mm, whereas the resolution along the centerline is roughly equal to the diameters of the focused laser beams, on the order of 0.1 mm.

Although the signal-to-noise ratio of the fluorescence signal might be improved by suitable filters, or by using a more sensitive detector, the photodiode signal was sufficiently strong that reasonable data could be obtained with phase-locked detection. Most of the data were taken with a total dye laser power of about 100 mW, with an estimated 20 mW in each beam in the plume. By increasing the power level momentarily, it was confirmed that no significant power broadening or saturation broadening of the measured Doppler profiles occurred.

To obtain measurements at different positions in the arcjet plume, the thruster itself was moved by the computer-controlled xyz stage. This has the important advantage that alignment of all optical components has to be performed only once. Particularly, alignment of the detection lens is critical to ensure that the overlap region of the two laser beams is imaged

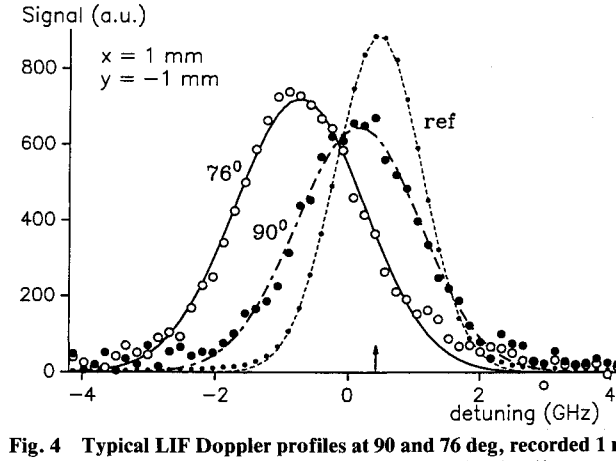

Fig. 4 Typical LIF Doppler profiles at 90 and 76 deg, recorded 1 mm downstream from the exit plane, 1 mm off centerline (on "upstream" side of laser beam). Gaussian curve fits are shown as well. The arrow indicates line center, as determined from the optogalvanic reference signal (rightmost curve).

correctly onto the pinhole on the photodiode. This alignment was performed by maneuvering a sharp needle point into the laser beams, giving rise to direct scatter of the laser beams onto the photodiode. The needle remained on the *xyz* stage at all times, so that alignment could be checked even after evacuation of the vacuum chamber.

Data Acquisition and Data Analysis

Desktop computers were used both for data acquisition and data analysis. Doppler profile scans (see Fig. 4) were accomplished by a single program that drives the laser scan frequency and reads the three phase-locked amplifier signals. Thus, a single Doppler scan consists of repeatedly incrementing the laser frequency by a set amount, waiting for the signals of the phase-locked amplifiers to equilibrate, and then reading, in quick succession, the three Doppler signals, repeating the process until the scan is complete.

Given the fluctuations in the arcjet plume, we chose rather slow scans, allowing the use of a 1-s time constant on the phase-locked amplifiers. Thus, the duration of a single, 8-GHz (0.27 cm^{-1}) scan was 2 min, yielding 52 data points per scan. Because of the plume fluctuations, the fitted mean velocities are accurate only to about 30 MHz (or 20 m/s), even for much larger numbers of samples per Doppler profile.

Data analysis was performed after completion of the measurements. A simplex least-squares fitting program was used to fit each of the three signals to a Gaussian model function as expressed in Eq. (7), yielding fitted values for the amplitude, width, and center of each profile. A typical example of the measured signals along with the Gaussian curve fits is shown in Fig. 4.

IV. Experimental Results

Two series of LIF measurements were carried out. First, radial scans were performed 1 mm downstream from the nozzle exit plane, in a horizontal plane through the arcjet centerline. These data were actually taken on two consecutive days, with excellent reproducibility. Second, axial scans of the arcjet plume were performed on centerline.

Radial Data near Exit Plane

Results of the radial scans at $x = 1$ mm are shown in Figs. 5–7. First, Fig. 5 shows the measured mean velocities, obtained from the laser beams at angles of 90 and 76 deg to the flow, and the axial velocity, constructed from these two sets of data using Eq. (13). The same data are also presented in Fig. 6 in the form of a vector velocity diagram. Whereas the axial velocity peaks on centerline at about 3 km/s, the radial velocity reaches its largest value—about 300 m/s—at a radius of about 2.5 mm. The corresponding variation in flow angle β, as defined by Eq. (14), is from 0 deg on the centerline to about 15 deg at the edges of the plume. By comparison, the half-angle of the conical diverging section of the nozzle is 20 deg. Although the flow is symmetric in the central region, significant deviations are observed outside of the radial boundary layer. In fact, some recirculation and backflow are observed on one side. We speculate that this effect is aggravated by the blunt shape of the arcjet nozzle.

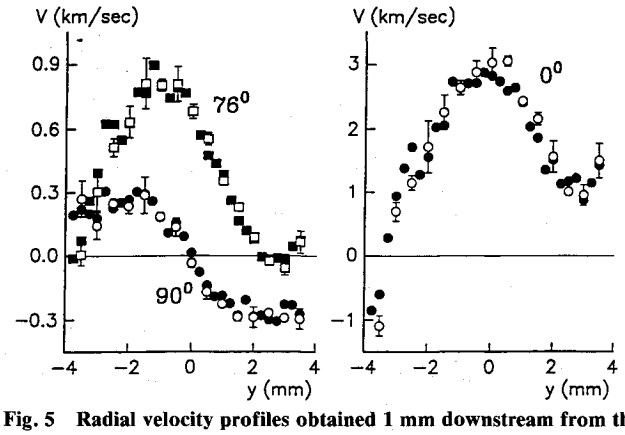

Fig. 5 Radial velocity profiles obtained 1 mm downstream from the exit plane. Data on the right are constructed from the two measured velocity components on the left. Open and closed symbols correspond to data sets taken on two consecutive days. Error bars on the open symbols were calculated from a series of three runs on the first day.

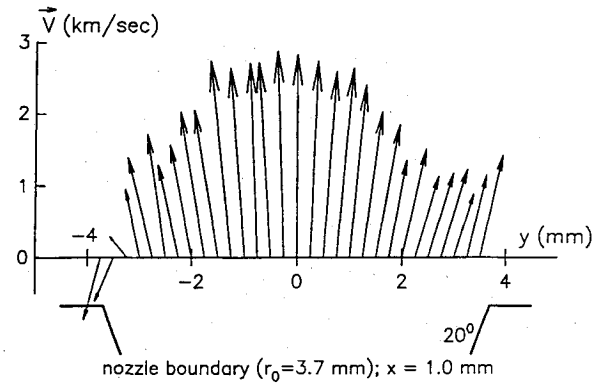

Fig. 6 Vector velocity diagram obtained from the data in Fig. 5 (using the data represented by the closed symbols only). The nozzle boundary is also indicated. Aspect ratios for velocity and length scales are chosen such that all angles are shown correctly.

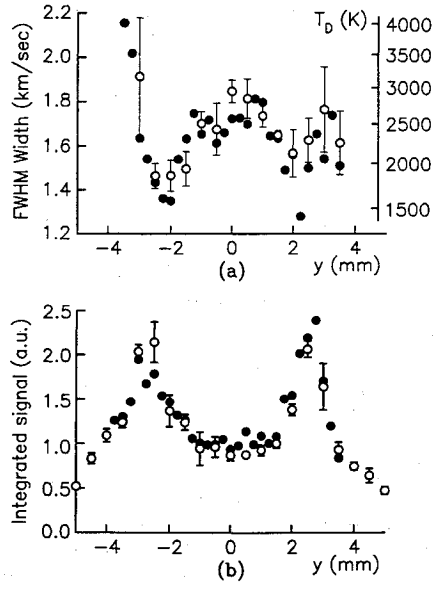

Fig. 7 Radial profiles of the average widths a) and average integrated signals b) of the data from Fig. 5. Both sets of data clearly indicate boundary-layer behavior at radii of about 2.3 mm, which is well within the 3.4-mm radius of the exit nozzle. A corresponding temperature scale is indicated in a) as well.

Widths and integrated signals for the same radial data are presented in Fig. 7. In both cases, the values that are shown are actually averages of the corresponding quantities from the Doppler profiles at 90 and at 76 deg. Although some differences between the two sets of data exist, the trends in the individual sets are largely the same as in Fig. 7. The most prominent features in Figs. 7a and 7b are those associated with the radial boundary layer at about 2.3 mm. In interpreting these data, it must be kept in mind that the species that is used in the LIF scheme is actually an excited state of the argon atom. Thus, although the peaks in the fluorescence signal appear to indicate sharp increases in the number density of the excited species in the boundary layer (presumably as a result of increased collision rates), they may not be representative for the bulk of the propellant gas. Moreover, it is possible that the increase in signal in the boundary layer is the result of a lower

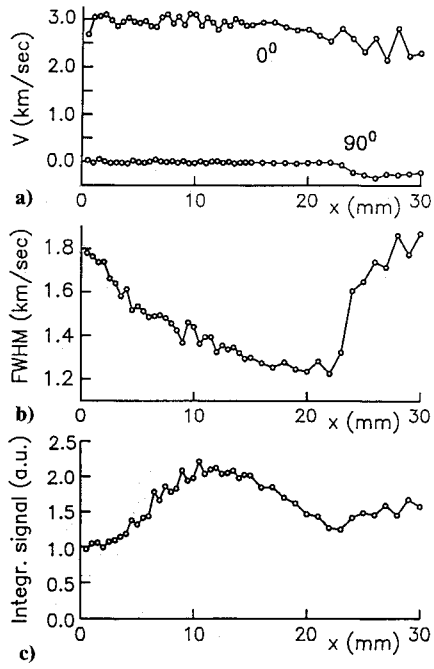

Fig. 8 Axial profiles of radial and axial velocity: a) average velocity spread, b) average integrated signal, and c) on centerline. All data reflect clearly the shock behavior that is observed visually as the crossing of two shock lines, 22 mm downstream from the exit plane (see Fig. 2).

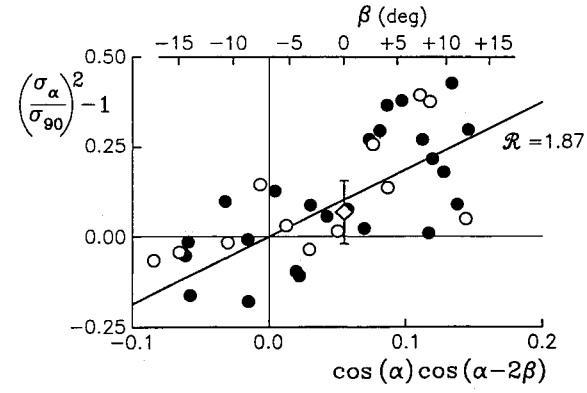

Fig. 9 Dependence of the Doppler width ratio $\sigma_\alpha/\sigma_{90}$ on the flow angle β for the data from Figs. 5–7. The data are curve fitted according to Eq. (15), yielding the slope $\Re = 1.87 \pm 0.28$. The diamond with error bar indicates the average and spread of the axial data from Fig. 8.

radiative quenching rate of the upper state because of a lower electron density and/or temperature there.

Still, some estimates can be obtained. The width of the velocity distribution on centerline is 1.8 km/s, which, with Eqs. (18), would give a maximum temperature of about 2800 K. This is an upper limit, because other broadening mechanisms might contribute to the observed Doppler widths, such as the recirculation outside the boundary layer, which is evident in Figs. 5 and 6. From the value of 2800 K and the value of 3 km/s for the peak velocity, it follows that the Mach number on centerline is about $M = 3.1 \pm 0.1$.

Axial Data on Centerline

A second series of data was taken on the arcjet centerline (see Fig. 8). Figure 8a shows the measured values of the radial velocity component and the deduced value of the axial component. The latter is remarkably constant throughout the expansion, dropping only slightly from the value of 3 km/s close to the exit nozzle. The radial component is negligible, as expected, until the position of the shock is reached at $x = 22$ mm (see Fig. 2).

Figure 8b shows that the Doppler width drops from an initial value of 1.8 km/s at the exit plane to about 1.25 km/s at the shock location. This corresponds to a drop in temperature from about 2800 to 1400 K and a rise in axial Mach number from $M = 3.0$ to 4.1. Behind the shock, the width rises rapidly to the original value of 1.8 km/s.

Finally, Fig. 8c shows the average integrated signals, which rise initially, then drop, and, at the location of the shock, continue to rise once more. Although a density increase following a shock is expected, the initial rise at the nozzle exit plane is more puzzling and may be the result of changing production rates of the excited species that is used in the LIF scheme.

Analysis of Flow Anisotropy

Although only average Doppler widths are shown in Figs. 7 and 8, some flow anisotropy was observed. This is illustrated in Fig. 9, which shows the correlation of Doppler width ratio and flow angle, in accordance with Eq. (15). Despite the scatter of the data, a correlation is evident, yielding a fit coefficient $\Re = 1.87 \pm 0.28$. According to the theory in Sec. II, this correlation can be explained in at least two ways. First, with Eq. (16), it would imply a variance ratio $(\sigma_\parallel/\sigma_\perp)^2 = 2.87$. Second, with Eq. (17), it would imply a ratio of 2.87 between the variance of the flow fluctuations to the variance of the instantaneous, isotropic velocity distribution. In light of the observed plume fluctuations, the latter explanation appears to be more plausible, although further work will be required to resolve the issue. For a more elaborate discussion on the observed flow anisotropy, we refer the reader to Ref. 20.

V. Discussion and Summary

We have demonstrated that an LIF technique, which has recently been employed to measure axial velocities in hydrazine and hydrogen arcjets, can be extended to measure radial and axial velocities in the arcjet plume simultaneously. Also, in addition to measuring vector velocity distributions in the plume, both qualitative and quantitative information can be extracted from the widths and integrated signals of the measured Doppler profiles. Particularly, the signatures of a radial boundary layer and an axial shock downstream from the exit nozzle are clearly evident in the data. Finally, we have demonstrated that simultaneous recording of the optogalvanic signal in a small discharge lamp is a very convenient method for establishing an absolute calibration of the Doppler shifts in the arcjet plume.

Although, in Refs. 14 and 15, only a qualitative discussion of the widths and strengths of the LIF signals is given, it appears that our data are qualitatively different from the work in Refs. 14 and 15 in that the LIF signals in our experiment are not largest on centerline but rather in the boundary layer at the edge of the plume. Qualitative agreement with the work in Refs. 14 and 15 was found in that the axial velocity is largest on centerline and drops off uniformly (at least, until the boundary layer is reached) with increasing radius. Extension of our two-beam multiplexing technique to the hydrogen Balmer-α line should be straightforward, although, as stated in Refs. 14 and 15, a somewhat more careful analysis would be required to take into account Stark broadening and broadening due to fine-structure components of the transition.

We conclude that we have successfully demonstrated that two-beam multiplexing can be used as a powerful diagnostic tool for characterizing two-component velocity distributions in an arcjet exhaust plume. Because of space limitations, some aspects of the measurements have not been discussed in much detail. These include some possible artifacts due to plume fluctuations, small systematic differences between the variances and integrated signal data of the two LIF signals, and non-Gaussian behavior of the velocity distribution near the boundary layer of the flow. For a more complete discussion, the reader is referred to Ref. 20.

Appendix

We describe here a simple model that can account for the different widths of the Doppler profiles at the two laser beam angles, based on the assumption that the magnitude of the mean flow velocity fluctuates with a characteristic frequency ω according to

$$\overline{v}(t) = \overline{v_0} + 2^{1/2}\,\overline{\Delta v}\cos\omega t \tag{A1}$$

where the mean velocity $\overline{v_0}$ is given by the mean average velocity components $\overline{v_x}$ and $\overline{v_y}$ from Eq. (2) according to $\overline{v_0}^2 = \overline{v_x}^2 + \overline{v_y}^2$, and $\overline{\Delta v}^2$ is the variance of the fluctuations with respect to temporal averaging. Repeating the calculation of the experimental Doppler profile that leads to Eqs. (7–10), and assuming an isotropic velocity distribution with variance σ^2, we find that the Doppler profile becomes time dependent, namely

$$S_\varphi(\nu_D, t) = A_\varphi \exp\left\{-\left[\frac{\nu_D - \nu_\varphi(t)}{\sigma}\right]^2\right\} \tag{A2}$$

where

$$\nu_\varphi(t) = (\overline{v_0} + 2^{1/2}\,\overline{\Delta v}\cos\omega t)\cos(\varphi - \beta) \tag{A3}$$

and where A_φ is given by Eq. (8), upon replacing σ_φ by σ. Note that, with the definition of the flow angle β from Eq. (14), Eq. (A3) reduces to Eq. (9) in the limit $\overline{\Delta v} = 0$. To carry out a temporal average of the time-dependent Doppler profile from Eq. (A2), we use the fact that, for small ϵ,

$$\langle \exp - (a + \epsilon\cos\omega t)^2\rangle \simeq \exp(-\tfrac{1}{2}\epsilon^2)\exp\left(\frac{-a^2}{1+\epsilon^2}\right)$$

where the brackets on the left indicate temporal averaging. With this, the temporally averaged Doppler profile from Eq. (A2) becomes

$$\langle S_\varphi(\nu_D, t)\rangle = A'_\varphi \exp\left[-\left(\frac{\nu_D - \overline{v_0}}{\sigma'}\right)^2\right] \tag{A4}$$

where

$$A'_\varphi = A_\varphi \exp\left[-\frac{\overline{\Delta v}^2}{2\sigma^2}\cos^2(\varphi - \beta)\right] \tag{A5}$$

and

$$\sigma'^2 = \sigma^2 = \overline{\Delta v}^2\cos^2(\varphi - \beta) \tag{A6}$$

Thus, as a result of temporal averaging, the Doppler profile is broadened and has a smaller amplitude. However, the integrated area under the Doppler profile is independent of the fluctuations, which follows from the fact that $A'_\varphi\sigma' = A_\varphi\sigma$ (to second order in $\overline{\Delta v}$), or, alternatively, from the observation that the order of integration and time averaging may be interchanged. Because the averaged quantities are independent of the oscillation frequency ω, they should be unaffected even in the case of more complex temporal fluctuations, as long as the variance $\overline{\Delta v}^2$ is the same.

Acknowledgments

This work was supported jointly by NASA under Grant NAGW-1195, the Air Force Office of Scientific Research under Grant AFOSR-91-0200, and Boeing Defense & Space Group, Seattle, Washington, with grant monitor J. Meserole. For technical assistance, we are much indebted to J. Hornkohl, C. Parigger, F. Schwartz, and, in particular, N. Wright. The first author gratefully acknowledges discussions with A. Eraslan, F. Collins, and J. Lewis. We also acknowledge assistance from T. Gogel and A. Sedghinasab in an early stage of this work.

References

[1]Beattie, J. R., and Penn, J. P., "Electric Propulsion—A National Capability," AIAA Paper 89-2240, June 1989.

[2]Reck, G. M., "NASA Directions in Space Propulsion for 2000 and Beyond," *Space Commercialization: Launch Vehicles and Programs,* edited by F. Shahroki, J. S. Greenberg, and T. Al-Saud, Vol. 126, Progress in Aeronautics and Astronautics, AIAA, Washington, DC, 1990, pp. 35–49.

[3]Jahn, R. G., *Physics of Electric Propulsion,* McGraw-Hill, New York, 1968, p. 9.

[4]Smith, R. D., Roberts, C. R., Davies, K., and Vaz, J., "Development and Demonstration of a 1.8 kW Hydrazine Arcjet Thruster," AIAA Paper 90-2547, July 1990.

[5]Knowles, S. C., Yano, S. E., and Aadland, R. S., "Qualification and Life Testing of a Flight Design Hydrazine Arcjet System," AIAA Paper 90-2576, July 1990.

[6]Rhodes, R. P., and Keefer, D., "Numerical Modeling of an Arcjet Thruster," AIAA Paper 90-2614, July 1990.

[7]Rhodes, R. P., and Keefer, D., "Modeling of a Hydrogen Arcjet Thruster," AIAA Paper 91-1994, June 1991.

[8]Tanaka, K., Tsuchiya, K., Kaita, K., and Nishida, M., "Computational Simulation of Arcjet Thruster Flow Fields," 3rd International Symposium on Computational Fluid Dynamics, Paper A90-25826, Nagoya, Japan, Aug. 1989.

[9]Zimmerman, M., and Miles, R. B., "Hypersonic-Helium-Flow-Field Measurements with the Resonant Doppler Velocimeter," *Applied Physics Letter,* Vol. 37, No. 10, 1980, pp. 885–887.

[10]Manzella, D. H., Curran, F. M., Myers, R. M., and Zube, D. M., "Preliminary Plume Characteristics of an Arcjet Thruster," AIAA Paper 90-2645, July 1990; also NASA TM-103241, July 1990.

[11]Tosti, E., Deininger, W. D., Mazzacurati, V., and Ruocco, G. C., "Arcjet Plume Analysis Using Emission Spectroscopy," 22nd International Electric Propulsion Conf., Paper 91-092, Viareggio, Italy, Oct. 1991.

[12]Bohn, W. L., Beth, M.-U., and Nedder, G., "On Spectroscopic Measurements of Velocity Profiles and Non-Equilibrium Radial Temperatures in an Argon Plasma Jet," *Journal of Quantitative Spectroscopy and Radiative Transfer,* Vol. 7, No. 4, 1967, pp. 661–676.

[13]Zube, D. M., and Myers, R. M., "Techniques for Spectroscopic Measurements in an Arcjet Nozzle," *Journal of Propulsion and Power,* Vol. 8, No. 1, 1992, pp. 254–256.

[14]Erwin, D. A., Pham-Van-Diep, G. C., and Deininger, W. D., "Laser-Induced Fluorescence Measurements of Flow Velocity in High-Power Arcjet Thruster Plumes," *AIAA Journal,* Vol. 29, No. 8, 1991, pp. 1298–1303.

[15]Liebeskind, J. G., Hanson, R. K., and Capelli, M. A., "Velocity Measurements in a Hydrogen Arcjet Using LIF," AIAA Paper 91-2112, June 1991.

[16]Liebeskind, J. G., Manzella, D. H., Ruthling, C. R., Hanson, R. K., and Capelli, M. A., "Optical Diagnostics of a Low Power Hydrogen Arcjet," 22nd International Electric Propulsion Conf., Paper 91-091, Viareggio, Italy, Oct. 1991.

[17]Liebeskind, J., Hanson, R., and Cappelli, M., "LIF of Atomic H in an Arcjet Thruster," 30th Aerospace Sciences Meeting, AIAA Paper 92-0678, Reno, NV, Jan. 1992.

[18]Cohen, R. B., and Welle, R., "Optical Diagnostics of Hydrogen Arcjets," 22nd International Electric Propulsion Conf., Paper 91-095, Viareggio, Italy, Oct. 1991.

[19]Ruyten, W. M., and Keefer, D., "Absolute Doppler Shift Calibration of Laser Induced Fluorescence Signals Using Optogalvanic Measurements in a Hollow Cathode Lamp," *Applied Physics Letters,* Vol. 61, No. 8, 1992, pp. 880–882.

[20]Ruyten, W. M., and Keefer, D., "Laser Fluorescence Velocimetry of an Arcjet Exhaust Plume," 22nd International Electric Propulsion Conference, Paper 91-093, Viareggio, Italy, Oct. 1991.

[21]Ruyten, W. M., and Keefer, D., "Characterization of Electric Thruster Plumes Using Multiplexed Laser Induced Fluorescence Measurements," AIAA Paper 92-2965, July 1992.

[22]Moeller, T., Rhodes, R., Keefer, D., Sedghi-Nasab, A., and Ruyten, W., "Comparison of Experimental and Numerical Results for an Argon Arcjet," AIAA Paper 92-3105, July 1992.

[23]Curran, F. M., and Sarmiento, C. J., "Low Power Arcjet Performance Characterization," AIAA Paper 90-2578, July 1990.

[24]Wiese, W. L., Smith, M. W., and Miles, B. M., *Atomic Transition Probabilities: Sodium through Calcium,* National Bureau of Standards, Government Printing Office, Washington, DC, Oct. 1969, p. 193.

[25]Keller, R. A., Engleman, R., Jr., and Zulewski, E. F., "Optogalvanic Spectroscopy in a Uranium Hollow Cathode Discharge," *Journal of the Optical Society of America,* Vol. 69, No. 5, 1979, p. 738.